



City Research Online

## City, University of London Institutional Repository

---

**Citation:** Bustos, A., Tomas-Rodriguez, M., Rubio, H. & Castejon, C. (2022). On the nonlinear hunting stability of a high-speed train bogie. *Nonlinear Dynamics*, doi: 10.1007/s11071-022-07937-y

This is the published version of the paper.

This version of the publication may differ from the final published version.

---

**Permanent repository link:** <https://openaccess.city.ac.uk/id/eprint/29127/>

**Link to published version:** <https://doi.org/10.1007/s11071-022-07937-y>

**Copyright:** City Research Online aims to make research outputs of City, University of London available to a wider audience. Copyright and Moral Rights remain with the author(s) and/or copyright holders. URLs from City Research Online may be freely distributed and linked to.

**Reuse:** Copies of full items can be used for personal research or study, educational, or not-for-profit purposes without prior permission or charge. Provided that the authors, title and full bibliographic details are credited, a hyperlink and/or URL is given for the original metadata page and the content is not changed in any way.

---

---

---

City Research Online:

<http://openaccess.city.ac.uk/>

[publications@city.ac.uk](mailto:publications@city.ac.uk)

---



# On the nonlinear hunting stability of a high-speed train bogie

Alejandro Bustos · Maria Tomas-Rodriguez · Higinio Rubio · Cristina Castejon

Received: 5 November 2021 / Accepted: 26 September 2022  
© The Author(s) 2022

**Abstract** The hunting phenomenon is an intrinsic swaying motion appearing in railway vehicles due to the vehicle's forward speed and the wheel–rail contact forces. Hunting motion consists of wheelset and other vehicle's components oscillations that arise above a certain vehicle's speed known as critical or hunting speed. These oscillations are of unstable nature and represent a safety hazard as they could lead to the vehicle's derailment. This article analyses the stability of a bogie nonlinear model for a Spanish high-speed train when this is travelling at speeds near the hunting speed. The vehicle's stability is studied by means of root loci methods, and the value of the critical speed is found. In addition to this, the behaviour of the vehicle

is studied in both stable and unstable regions and the existence of limit cycles is discussed in this work. Finally, a sensitivity analysis of the axle load and suspension parameters is performed. The results show that the axle load, the vertical stiffness of the primary suspension and the lateral damping of the secondary suspension have a significant influence on the value of the critical speed.

**Keywords** Nonlinear system · High-speed train · Vehicle stability dynamics · Numerical simulation

## Abbreviations

HST	High-speed train
$a$	Semixis of contact ellipse in longitudinal direction
$b$	Semixis of contact ellipse in lateral direction
$b_1$	Lateral distance between bogie frame centre of gravity and primary suspension longitudinal springs and dampers
$b_2$	Lateral distance between bogie frame centre of gravity and secondary suspension longitudinal springs
$b_3$	Lateral distance between bogie frame centre of gravity and secondary suspension longitudinal springs
$c_{11}$	Kalker's coefficient
$c_{22}$	Kalker's coefficient
$c_{23}$	Kalker's coefficient
$c_{33}$	Kalker's coefficient

---

A. Bustos (✉)  
MAQLAB Research Group, Department of Mechanics,  
UNED, C/Juan del Rosal, 12, 28040 Madrid, Spain  
e-mail: albustos@ind.uned.es

M. Tomas-Rodriguez  
Department of Mechanical Engineering and Aeronautics,  
The City, University of London, Northampton Square,  
London EC1V 0HB, UK  
e-mail: Maria.Tomas-Rodriguez.1@city.ac.uk

H. Rubio · C. Castejon  
MAQLAB Research Group, Department of Mechanical  
Engineering, Universidad Carlos III de Madrid, Av. de la  
Universidad, 30, 28911 Leganes, Madrid, Spain  
e-mail: hrbio@ing.uc3m.es

C. Castejon  
e-mail: castejon@ing.uc3m.es

$C_{px}$	Longitudinal primary suspension damping	$L_1$	Longitudinal distance between bogie frame centre of gravity and primary suspension lateral springs
$C_{py}$	Lateral primary suspension damping	$L_2$	Longitudinal distance between bogie frame centre of gravity and primary suspension lateral dampers
$C_{pz}$	Vertical primary suspension damping	$m_b$	Bogie frame mass
$C_{sx}$	Longitudinal secondary suspension damping	$M_{Lxi}$	Creep torque at left wheel of wheelset $i$ along longitudinal direction
$C_{sy}$	Longitudinal secondary suspension damping	$M_{Lzi}$	Creep torque at left wheel of wheelset $i$ along vertical direction
$e$	Half of the track gauge	$M_{Rxi}$	Creep torque at right wheel of wheelset $i$ along longitudinal direction
$f_{11}$	Lateral creep force coefficient	$M_{Rzi}$	Creep torque at right wheel of wheelset $i$ along vertical direction
$f_{12}$	Lateral/spin creep force coefficient	$M_{szb}$	Secondary suspension torques
$f_{22}$	Spin creep force coefficient	$M_{szi}$	Suspension torque of wheelset $i$ along vertical direction
$f_{33}$	Longitudinal creep force coefficient	$m_w$	Wheelset mass
$F_{Lxi}$	Longitudinal creep force of the left wheel of the wheelset $i$	$N_{Ly_i}$	Lateral component of the normal force at left wheel of wheelset $i$
$F_{Lyi}$	Lateral creep force of the left wheel of the wheelset $i$	$N_{Lz_i}$	Vertical component of the normal force at left wheel of wheelset $i$
$F_{Lzi}$	Vertical creep force of the left wheel of the wheelset $i$	$N_{Ry_i}$	Lateral component of the normal force at right wheel of wheelset $i$
$F_{Rxi}$	Longitudinal creep force of the right wheel of the wheelset $i$	$N_{Rz_i}$	Vertical component of the normal force at right wheel of wheelset $i$
$F_{Ryi}$	Lateral creep force of the right wheel of the wheelset $i$	$r_0$	Wheel radius
$F_{Rzi}$	Vertical creep force of the right wheel of the wheelset $i$	$r_L$	Rolling radius of left wheel
$F_{syb}$	Secondary suspension forces	$R_{Lxi}$	Longitudinal component of position vector on left wheel of wheelset $i$
$F_{szi}$	Force of the secondary suspension in vertical direction	$R_{Ly_i}$	Lateral component of position vector on left wheel of wheelset $i$
$F_{ti}$	Flange contact forces	$R_{Lz_i}$	Vertical component of position vector on left wheel of wheelset $i$
$G$	Shear modulus of steel	$r_R$	Rolling radius of right wheel
$g$	Ratio of contact axes	$R_{Rxi}$	Longitudinal component of position vector on right wheel of wheelset $i$
$h_1$	Vertical distance between the wheelset and the secondary suspension damper	$R_{Ry_i}$	Lateral component of position vector on right wheel of wheelset $i$
$h_2$	Vertical distance between the wheelset and the secondary suspension spring	$R_{Rz_i}$	Vertical component of position vector on right wheel of wheelset $i$
$i$	Wheelset index ( $i = 1$ for front wheelset, $i = 2$ for rear wheelset)	$V$	Forward speed of bogie
$I_{bz}$	Moment of inertia of the bogie frame around yaw axis	$W_{pa}$	Axle load
$I_{wx}$	Moment of inertia of the wheelset inertia around roll axis	$y_i$	Lateral displacement of wheelset $i$
$I_{wy}$	Moment of inertia of the wheelset inertia around pitch axis	$z_i$	Vertical displacement of wheelset $i$
$I_{wz}$	Moment of inertia of the wheelset inertia around yaw axis	$\alpha$	Creepage saturation coefficient
$K_{px}$	Longitudinal primary suspension stiffness	$\delta$	Flange clearance
$K_{py}$	Lateral primary suspension stiffness		
$K_{pz}$	Vertical primary suspension stiffness		
$K_r$	Rail stiffness		
$K_{sx}$	Longitudinal secondary suspension stiffness		
$K_{sy}$	Lateral secondary suspension stiffness		

$\delta_L$	Contact angle of left wheel
$\delta_R$	Contact angle of right wheel
$\lambda$	Wheel conicity
$\nu$	Poisson ratio of steel
$\varphi_i$	Roll angle of wheelset $i$
$\psi_i$	Yaw angle of wheelset $i$

## 1 Introduction

Railway transport plays a key role in the worldwide economy. The last available data from the European Union show that railway transport made a turnover of more than 68 billion € in 2017 and transported 407 billion passengers per kilometre in 2018 [1]. Over the decades, in many cases, the development of the high-speed rail has made the train a convenient alternative to the aircraft for journeys up to 1000 km long [2]. This has a beneficial impact on CO<sub>2</sub> and greenhouse gas reduction due to the electric nature of high-speed trains (HST) [3].

A key aspect to guaranteeing the comfort and the safety of a railway vehicle is to ensure its stability at all stages of travel. For this, it is necessary to determine the velocity at which the train's motion becomes unstable. The conic shape of the wheels rigidly mounted on the axle leads to an inherent lateral displacement on rail vehicles called hunting motion. At low speeds, hunting motion consists of well-damped small amplitude oscillations. However, when the speed is increased up to a certain value, this oscillation (hunting motion) becomes unstable with growing amplitude oscillations. The lowest speed at which this phenomenon occurs is called *critical speed* [4]. When this happens, the contact between the wheel flanges and the rails limits the amplitude of the oscillations, keeping the bogie within the track. If the motion is too violent, the oscillations amplitude increases and the flange–rail contact may become insufficient to maintain the railway vehicle on the track and a derailment can happen.

According to Polach [5], bogie stability can be determined by three methods according to the values analysed: wheelset displacement, forces between wheelset and track, and lateral acceleration on the bogie frame. The two latter require actual measures on track, while the first method can be applied from both

track measurements or simulation results. The combination of wheelset displacement with other mathematical methods is the preferred method for establishing the critical speed in the scientific literature. For example, Schupp [6] studies the critical speed of a high-speed train by analysing its lateral displacement with the help of bifurcation analysis, root locus and limit cycles. A similar approach is used by Zboinski and Dusza [7] for investigating the performance of two 4-axle rail vehicles on curved tracks. Rezvani and Mazraeh [8] study the effects of varying the axle box clearances, the wheel–rail friction coefficient and the curve radius on the critical speed of a freight wagon. They also use the wheelset lateral displacement as a parameter to establish the critical speed.

The use of commercial software (as the three previous works do) makes easier the task of modifying the rail vehicles and analysing the impact of these changes in the critical speed. However, most published researches use algorithms developed by the authors to study rail vehicles. Both linear [9–12] and nonlinear models [13, 14] can be found in the literature. It is a standard practice that linear models have as a starting point a set of nonlinear equations that are linearized around an equilibrium point. This is the case of the approach used by Lee et al. [15] and [16], where the authors present the nonlinear equations of a complex bogie model and then linearize them to investigate the influence of several parameters on the bogie's performance in straight and curved tracks. Linear models are also used to study the behaviour of rail bogies in non-standard conditions. For example, Yao et al. [17] use a linear model of a bogie equipped with an active mass inertial actuator that controls lateral vibration improving the bogie's hunting stability. Sun et al. [18] analyse the effect of a defective yaw damper on the critical speed of the bogie and, hence, its stability. Other models although being represented by linear equations, use nonlinear expressions to describe the contact forces [11, 19, 20]. In this way, the performance of the railway vehicle as a function of the wheel–rail contact model can be studied accurately.

On the other hand, full nonlinear models take into account the couplings existing between the different DOF and nonlinear effects derived from mechanical elements. Bosso et al. [21] perform a stability analysis of a bi-dimensional model of the friction dampers used in the Y25 freight bogie. Molatefi [22] proposes a

mathematical model for studying the stability of a freight wagon which includes several nonlinear effects such as nonlinear springs and clearances. It is well-known and has been proved that for any given bogie model, if a linear approximation is used to determine the critical speed, the result is always higher than the critical speed that would be determined by using a nonlinear representation of the model [7, 23, 24]. This phenomenon is an important issue to consider when designing and implementing control methods for bogie stability as a linear model can lead to overconfident estimations of the stability limits on the vehicle.

In this paper, a 10-DOF nonlinear model of a high-speed bogie is developed and analysed as the first step for the development of a digital twin (DT) of a bogie for maintenance purposes. As Cerutti et al. highlight in [25], the stages to be covered in a DT are the modelling and simulation of the physical system to create a virtual model, data fusion obtained from different sensors on the physical system, interaction and collaboration between the physical system and the DT through sensors and actuators and application in service. In this sense, in order to develop a DT of the rolling stock, a previous parameterized model is needed and developed in this research. First, the dynamic behaviour of the bogie is analysed for a wide speed range. The critical speed is computed and then a sensitivity analysis is performed to understand the influence of the axle load and primary and secondary suspension parameters in the critical speed. Based on this sensitivity analysis, those suspension components which may have the greatest influence on the stability

of the bogie, and therefore are more likely to compromise the safety of the high-speed train, shall be identified. The analysis methods used in this work study the stability of a nonlinear model by means of the frozen eigenvalues approach. This is an extensively used approach in the research community due to various advantages: nonlinear systems stability can be approached by linear methods, more straight forward implementation and is more computationally efficient.

The structure of the paper is as follows: The following section describes the specific trailer bogie and wheelset under study. Section 3 details the mathematical model used for the analysis. It consists of a 10 DOF model yielding a set of nonlinear differential equations. Section 4 studies the stability limits of the vehicle and determines the hunting speed for this type of train. Section 5 shows the hunting speed sensitivity to axle load, primary and secondary suspension changes. Section 6 contains the conclusions of this work as well as further research suggestions.

## 2 Bogie description

The trailer bogie under study in this work belongs to a Spanish high-speed train (HST) that started to operate in 1992. The type of bogie studied is widely used in HSTs across Europe and other countries. Around the world, more than 450 trainsets use this type of bogie. It is designed to withstand axle loads of up to 17 tons at speeds exceeding 300 km/h.

Each trainset is composed of two power cars (M1 and M2) and eight passenger cars (R1-R8). Each power car seats on two bogies and each passenger car seats on two shared bogies (Fig. 2).

The distance between the bogie axles is 3000 mm, which provides the train with a considerably high critical speed and good stability properties for a wide range of running conditions. The bogie under study is shown in Fig. 3, and its position within the trainset is shown in Fig. 2.

Each wheelset contains a solid axle, two wheels of nominal diameter 920 mm and four disc brakes. The primary suspension of the trailer bogies consists of concentric helical springs and a vertical damper between the axle box and the bogie frame. The main secondary suspension is pneumatic, although it also



**Fig. 1** Spanish high-speed train, Atocha Station, Madrid, Spain [author's repository]

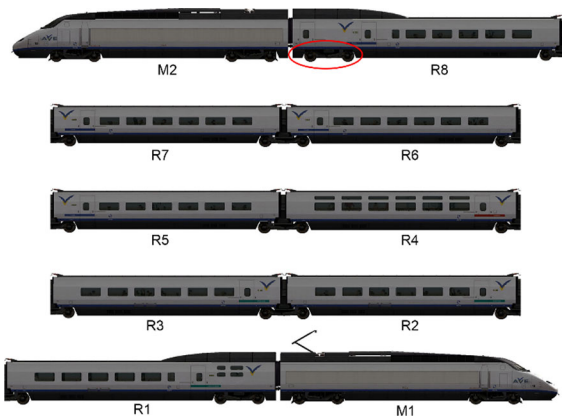


**Fig. 2** Trainset diagram with the studied bogie circled in R8

has hydraulic dampers in the longitudinal, lateral and vertical directions.

The parameters of Table 1 are used to create the bogie model. These data have been obtained from the manufacturers’ technical documentation within the joint research project in which the authors participate.

### 3 Mathematical model

In order to carry out stability studies for the high-speed train bogie mentioned in the previous section, a ten-degree-of-freedom (DOF) model following the approach presented in [15, 26] is derived. This model considers both the frame and wheelsets’ dynamics: lateral and vertical motions, yaw and roll angles for each of the two wheelsets, and the lateral displacement and yaw angle of the bogie frame. A schematic configuration of the bogie is shown in Figs. 4 and 5.

The forces and moments acting on each wheelset “*i*” are shown in the free body diagram in Fig. 6:  $F_{sy}$  and  $F_{sz}$  are the forces due to the primary suspension, and  $M_{sx}$  and  $M_{sz}$  are the torques due to the primary suspension too.  $W_i$  is the wheelset weight,  $N_R$  and  $N_L$  are the normal forces in the wheel–rail contact point, and  $F_R$  and  $F_L$  are the creep forces generated on the wheel–rail contact.

The bogie’s frame lateral motion  $y_b$  and yaw angle  $\psi_b$  are given in Eqs. (1) and (2).  $m_b$  is the frame mass,  $I_{bz}$  is the moment of inertia around the yaw axis,  $F_{syb}$  is the total balance of forces acting on the bogie’s  $y$ -axis, and  $M_{szb}$  represents the total balance of moments acting on the bogie around the  $z$ -axis:

$$m_b \ddot{y}_b = F_{syb} \tag{1}$$

$$I_{bz} \ddot{\psi}_b = M_{szb} \tag{2}$$

Equations (3)–(6) describe the lateral  $y_i$  and vertical  $z_i$  displacements, yaw  $\psi_i$  and roll  $\phi_i$  angles for each wheelset. The subscript  $i$  refers to the front and rear wheelsets on each bogie and takes values  $i = 1$  for the front wheelset and  $i = 2$  for the rear wheelset [11].

$$m_w \ddot{y}_i = F_{Ly_i} + F_{Ry_i} + N_{Ly_i} + N_{Ry_i} + F_{sy_i} - F_{ti} \tag{3}$$

$$m_w \ddot{z}_i = F_{Lz_i} + F_{Rz_i} + N_{Lz_i} + N_{Rz_i} + F_{sz_i} - W_{pa} \tag{4}$$

$$I_{wz} \ddot{\psi}_i = -I_{wy} \frac{V}{r_0} \dot{\phi}_i + (R_{Rxi} F_{Ry_i} - R_{Ryi} F_{Rxi}) + (R_{Lxi} F_{Ly_i} - R_{Ly_i} F_{Lxi}) + (R_{Rxi} N_{Ry_i} - R_{Lxi} N_{Ly_i}) + M_{Lz_i} + M_{Rz_i} + M_{sz_i} \tag{5}$$

$$I_{wx} \ddot{\phi}_i = -I_{wy} \frac{V}{r_0} \dot{\psi}_i + (R_{Ryi} F_{Rz_i} - R_{Rzi} F_{Ryi}) + (R_{Ly_i} F_{Lz_i} - R_{Lz_i} F_{Ly_i}) + (R_{Ly_i} N_{Lz_i} + R_{Ryi} N_{Rz_i}) - (R_{Rz_i} N_{Ry_i} + R_{Lz_i} N_{Lz_i}) + M_{Lx_i} + M_{Rx_i} + M_{sx_i} \tag{6}$$

$m_w$ ,  $I_{wz}$  and  $I_{wx}$  are the wheelset mass and the wheelset moments of inertia about the  $z$  and  $x$ -axis, respectively.  $V$  is the bogie’s forward speed, and  $W_{pa}$  is the axle load. Note that there are two wheelsets  $i = \{1,2\}$ ; therefore, the mathematical model consists of frame dynamics Eqs. (1)–(2), and two sets of Eqs. (3)–(6), being this a total of ten second-order differential equations. The parameters in Eqs. (1)–(6) will be derived in the following lines.

In order to compute the contact forces that exist between the wheel and the rail, the authors make use of Kalker’s linear theory yielding Eqs. (7)–(10):

$$f_{11} = abGc_{22} \tag{7}$$

$$f_{12} = (ab)^{3/2} Gc_{23} \tag{8}$$

$$f_{22} = (ab)^2 Gc_{33} \tag{9}$$

$$f_{33} = abGc_{11} \tag{10}$$

Parameters  $a$  and  $b$  are the semi-axes of the contact ellipse obtained following Hertz’s theory [27, 28].  $G$  is the steel’s shear modulus and,  $c_{11}$ ,  $c_{22}$ ,  $c_{23}$  and  $c_{33}$  are the Kalker’s coefficients (see [29] for further details):



**Table 1** Model parameters

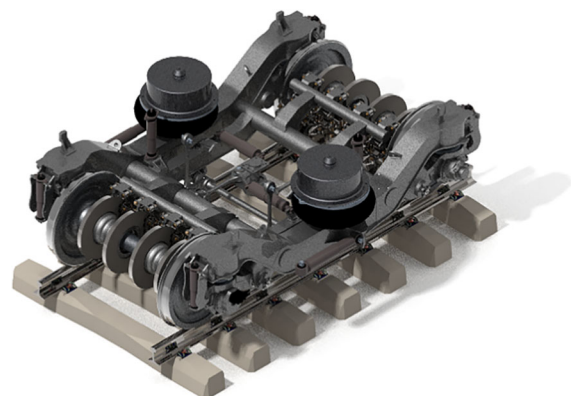
Parameter	Symbol	Value
Bogie frame mass	$m_b$	1610 kg
Bogie frame moment of inertia around yaw axis	$I_{bz}$	$2.82 \times 10^3 \text{ kg m}^2$
Wheelset mass	$m_w$	1570 kg
Wheelset moment of inertia around roll axis	$I_{wx}$	$693 \text{ kg m}^2$
Wheelset moment of inertia around pitch axis	$I_{wy}$	$121 \text{ kg m}^2$
Wheelset moment of inertia around yaw axis	$I_{wz}$	$693 \text{ kg m}^2$
Long. distance between bogie frame CG and primary suspension lateral springs	$L_1$	1.5 m
Long. distance between bogie frame CG and primary suspension lateral dampers	$L_2$	1.5 m
Lateral distance between bogie frame CG and primary suspension longitudinal springs /dampers	$b_1$	1.02 m
Lateral distance between bogie frame CG and secondary suspension longitudinal springs	$b_2$	1.04 m
Lateral distance between bogie frame CG and secondary suspension longitudinal springs	$b_3$	1.34 m
Vertical distance wheelset and secondary suspension damper	$H_1$	0.42 m
Vertical distance wheelset and secondary suspension spring	$H_2$	0.14 m
Axle load	$W_{pa}$	$15 \times 10^3 \text{ kg}$
Half of the track gauge	$e$	0.7175 m
Wheel radius	$r_0$	0.46 m
Wheel conicity	$\lambda$	0.025
Longitudinal primary suspension stiffness	$K_{px}$	$5.8 \times 10^7 \text{ N/m}$
Lateral primary suspension stiffness	$K_{py}$	$1.6 \times 10^7 \text{ N/m}$
Vertical primary suspension stiffness	$K_{pz}$	$5.4 \times 10^5 \text{ N/m}$
Longitudinal primary suspension damping	$C_{px}$	0 Ns/m
Lateral primary suspension damping	$C_{py}$	0 Ns/m
Vertical primary suspension damping	$C_{pz}$	5 kNs/m
Longitudinal secondary suspension stiffness	$K_{sx}$	$10^5 \text{ N/m}$
Lateral secondary suspension stiffness	$K_{sy}$	$10^5 \text{ N/m}$
Longitudinal secondary suspension damping	$C_{sx}$	$1.3 \times 10^4 \text{ Ns/m}$
Longitudinal secondary suspension damping	$C_{sy}$	$3 \times 10^4 \text{ Ns/m}$
Rail stiffness	$K_r$	$1.617 \times 10^7 \text{ N/m}$
Flange clearance	$\delta$	0.009 m

$$c_{11} = 2.39 + 2.338v + 1.014g + 2.736v^2 - 0.0728vg - 0.0139g^2 \quad (11)$$

$$c_{22} = 2.353 - 0.0212v + 1.074g + 1.163 - 0.0319g^2 \quad (12)$$

$$c_{23} = 0.2866 + 0.4467v + 1.049g + 0.038vg - 0.0177g^2 + 0.005g^3 + 0.1479g^2v \quad (13)$$

$$c_{33} = 0.7375 - 1.177v + 0.4506g + 1.076vg - 0.023g^2 \quad (14)$$

**Fig. 3** HST bogie CAD 3D view



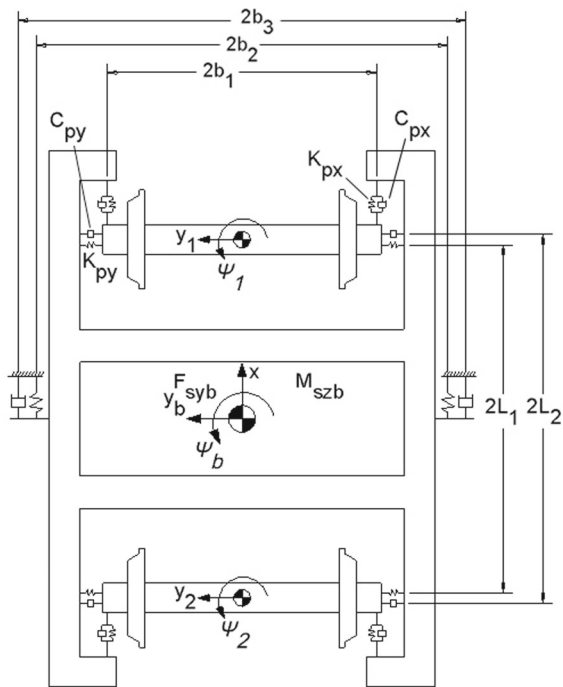


Fig. 4 Bogie model (top view)

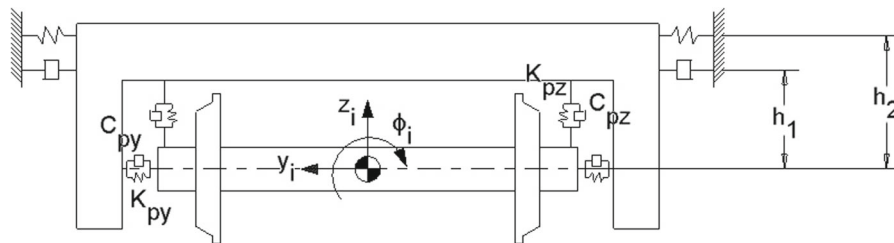
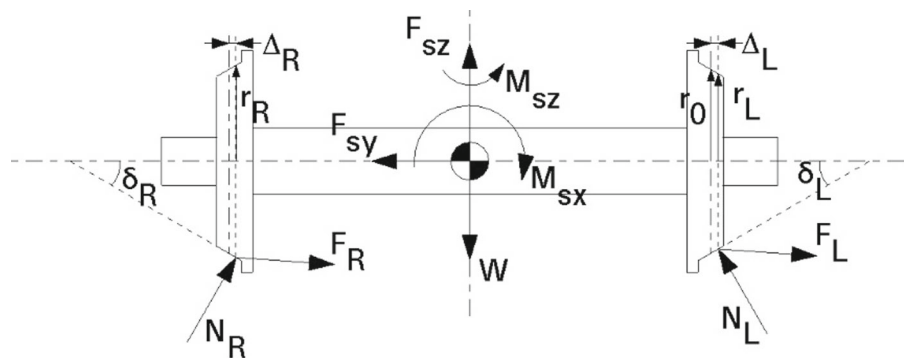


Fig. 5 Bogie model (front view)

Fig. 6 Free body diagram of a wheelset



where  $\nu$  is the steel Poisson ratio and  $g$  is the ratio between the semi-axes of the contact ellipse,  $a/b$ .

On the other hand, the conical wheel seating on a knife-edge rail is modelled as a linear constraint function relating the wheel and rail geometries:

$$\delta_L = \delta_R = \lambda, \quad \frac{1}{2}(r_L - r_R) = \lambda y_i, \quad \frac{1}{2}(r_L + r_R) = r_0 \quad (15)$$

$\delta_L, \delta_R$  are the respective left and right wheels' conicity angles and  $\lambda$  is the approximated conicity angle obtained by small-angle approximation.  $r_L, r_R$  are the left and right cone radius,  $r_0$  is the wheel's nominal radius and  $y_i$  is the corresponding wheelset "i" lateral displacement.

Creep forces and moments for each wheelset can be calculated following the approach in Garg and Dukkipati [26] where creepage saturation [28, 30] introduces nonlinearities in the model. Equations (16)–(20) represent the creep forces along the  $x, y$  and  $z$  axes and moments around the  $x$  and  $z$  axes for the left wheel ( $L$ ) on each wheelset  $i$ :

$$F_{Lxi} = -\frac{\alpha_{if33}}{V} \left[ V \left( 1 - \frac{r_L}{r_0} \right) - e\dot{\psi}_i \right] - \left[ -\frac{\alpha_{if11}}{V} [\dot{y}_i + r_L\dot{\phi}_i - V\psi_i] - \frac{\alpha_{if12}}{V} \left[ \psi_i - \frac{V}{r_0} \delta_L \right] \right] \psi_i \tag{16}$$

$$F_{Lyi} = -\frac{\alpha_{if33}}{V} \left[ V \left( 1 - \frac{r_L}{r_0} \right) - e\dot{\psi}_i \right] \psi_i + \left[ -\frac{\alpha_{if11}}{V} [\dot{y}_i + r_L\dot{\phi}_i - V\psi_i] - \frac{\alpha_{if12}}{V} \left[ \psi_i - \frac{V}{r_0} \delta_L \right] \right] \tag{17}$$

$$F_{Lzi} = \left[ -\frac{\alpha_{if11}}{V} [\dot{y}_i + r_L\dot{\phi}_i - V\psi_i] - \frac{\alpha_{if12}}{V} \left[ \psi_i - \frac{V}{r_0} \delta_L \right] \right] (\delta_L + \phi_i) \tag{18}$$

$$M_{Lxi} = \left[ \frac{\alpha_{if12}}{V} [\dot{y}_i + r_L\dot{\phi}_i - V\psi_i] - \frac{\alpha_{if22}}{V} \left[ \dot{\psi}_i - \frac{V}{r_0} \delta_L \right] \right] (\delta_L + \phi_i) \psi_i \tag{19}$$

$$M_{Lzi} = \frac{\alpha_{if12}}{V} [\dot{y}_i + r_L\dot{\phi}_i - V\psi_i] - \frac{\alpha_{if22}}{V} \left[ \dot{\psi}_i - \frac{V}{r_0} \delta_L \right] \tag{20}$$

Similarly, creep forces and moments appearing on the right wheel (*R*) of each wheelset *i* are given in the following expressions (21)–(25):

$$F_{Rxi} = -\frac{\alpha_{if33}}{V} \left[ V \left( 1 - \frac{r_R}{r_0} \right) + e\dot{\psi}_i \right] + \left[ \frac{\alpha_{if11}}{V} [\dot{y}_i + r_R\dot{\phi}_i - V\psi_i] + \frac{\alpha_{if12}}{V} \left[ \psi_i + \frac{V}{r_0} \delta_R \right] \right] \psi_i \tag{21}$$

$$F_{Ryi} = -\frac{\alpha_{if33}}{V} \left[ V \left( 1 - \frac{r_R}{r_0} \right) + e\dot{\psi}_i \right] \psi_i - \left[ \frac{\alpha_{if11}}{V} [\dot{y}_i + r_R\dot{\phi}_i - V\psi_i] + \frac{\alpha_{if12}}{V} \left[ \psi_i + \frac{V}{r_0} \delta_R \right] \right] \tag{22}$$

$$F_{Rzi} = -\left[ -\frac{\alpha_{if11}}{V} [\dot{y}_i + r_L\dot{\phi}_i - V\psi_i] - \frac{\alpha_{if12}}{V} \left[ \psi_i + \frac{V}{r_0} \delta_L \right] \right] (\delta_R - \phi_i) \tag{23}$$

$$M_{Rxi} = -\left[ \frac{\alpha_{if12}}{V} [\dot{y}_i + r_R\dot{\phi}_i - V\psi_i] - \frac{\alpha_{if22}}{V} \left[ \dot{\psi}_i + \frac{V}{r_0} \delta_R \right] \right] (\delta_R - \phi_i) \psi_i \tag{24}$$

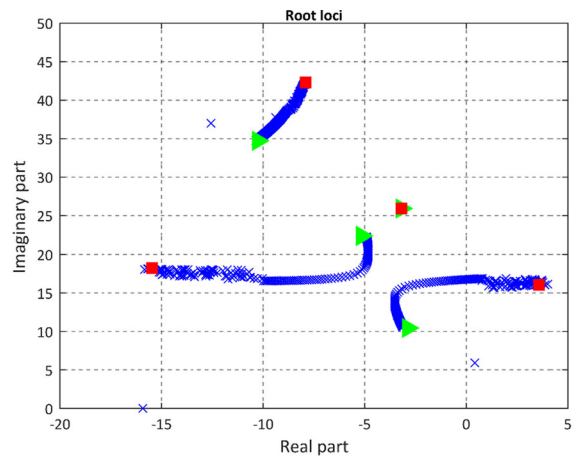


**Fig. 7** HST bogie root loci from initial speed  $v_i = 300$  km/h (►) up to  $v_f = 600$  km/h (◻)

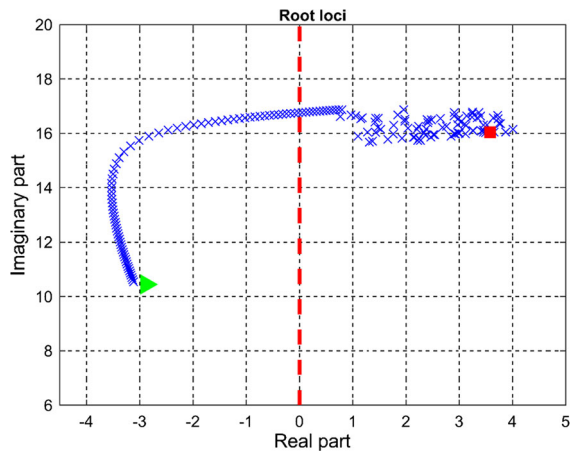


**Fig. 8** HST bogie root loci from initial speed  $v_i = 300$  km/h (►) up to  $v_f = 600$  km/h (◻)

$$M_{Rzi} = \frac{\alpha_{if12}}{V} [\dot{y}_i + r_R\dot{\phi}_i - V\psi_i] - \frac{\alpha_{if22}}{V} \left[ \dot{\psi}_i + \frac{V}{r_0} \delta_R \right] \tag{25}$$

$\alpha_i$  is the saturation coefficient for each wheelset and it is found as follows:

$$\alpha_i = \begin{cases} \frac{1}{\beta_i} \left[ \beta_i - \frac{1}{3}\beta_i^2 + \frac{1}{27}\beta_i^3 \right] & \text{for } \beta_i \leq 3 \\ \beta_i & \text{for } \beta_i > 3 \end{cases} \tag{26}$$

and  $\beta_i$  is used to calculate saturation for the creep forces as stated by Eqs. (27)–(30):

$$\beta_i = \frac{\beta_{iL} + \beta_{iR}}{2} \tag{27}$$

$$\beta_{ij} = \frac{\sqrt{F_{xlin-ij}^2 + F_{ylin-ij}^2}}{\mu N}, j = \{L, R\} \tag{28}$$

$$F_{xlin-ij} = -f_{33}\xi_{x-ij} \tag{29}$$

$$F_{ylin-ij} = -f_{11}\xi_{y-ij} - f_{12}\xi_{sp-ij} \tag{30}$$

$\xi_x$ ,  $\xi_y$  and  $\xi_{sp}$  are the longitudinal, lateral and spin creepages, respectively, calculated for left and right wheels as follows:

$$\begin{aligned} \text{Left wheel : } \xi_{xL} &= \frac{1}{V} \left[ V \left( 1 - \frac{r_L}{r_0} \right) - e\dot{\psi} \right], \\ \xi_{yL} &= \frac{1}{V} \left[ \dot{y} + r_L\dot{\phi} - V\psi \right], \xi_{spL} = \frac{1}{V} \left[ \dot{\psi} - \frac{V}{r_0}\delta_L \right] \end{aligned}$$

$$\begin{aligned} \text{Right wheel : } \xi_{xR} &= \frac{1}{V} \left[ V \left( 1 - \frac{r_R}{r_0} \right) + e\dot{\psi} \right], \\ \xi_{yR} &= \frac{1}{V} \left[ \dot{y} + r_R\dot{\phi} - V\psi \right], \xi_{spR} = \frac{1}{V} \left[ \dot{\psi} + \frac{V}{r_0}\delta_R \right] \end{aligned}$$

The position vectors of the contact points are indicated in Eqs. (31–36) assuming the displacements from the equilibrium position are small enough and are equal to the half of the track gauge:

$$R_{Rxi} = e\psi_i \tag{31}$$

$$R_{Ryi} = -e + r_R\phi_i \tag{32}$$

$$R_{Rzi} = -e\phi_i - r_R \tag{33}$$

$$R_{Lxi} = -e\psi_i \tag{34}$$

$$R_{Lyi} = e + r_L\phi_i \tag{35}$$

$$R_{Lzi} = e\phi_i - r_L \tag{36}$$

The normal forces of the left and right wheels in the vertical direction are:

$$N_{Lzi} = N_{Rzi} = \frac{1}{2} W_{pa} \tag{37}$$

The normal forces of the left and right wheels in the lateral direction are:

$$N_{Lyi} = -N_{Lzi} \tan(\delta_L + \phi_i) \approx -\frac{1}{2} W_{pa}(\delta_L + \phi_i) \tag{38}$$

$$N_{Ryi} = N_{Rzi} \tan(\delta_L + \phi_i) \approx \frac{1}{2} W_{pa}(\delta_R - \phi_i) \tag{39}$$

Therefore, the forces and moments acting on the wheelsets are now given by Eqs. (40)–(43):

$$\begin{aligned} F_{syi} &= -2K_{py}y_i - 2C_{py}\dot{y}_i + 2K_{py}y_b \\ &\quad + 2C_{py}\dot{y}_b - (-1)^i K_{py}L_1\psi_b - (-1)^i C_{py}L_1\dot{\psi}_b \end{aligned} \tag{40}$$

$$F_{szi} = -2K_{pz}z_i - 2C_{pz}\dot{z}_i \tag{41}$$

$$\begin{aligned} M_{szi} &= -2K_{px}b_1^2\psi_i + -2C_{px}b_1^2\dot{\psi}_i + 2b_1^2K_{px}\psi_b \\ &\quad + 2C_{px}b_1^2\dot{\psi}_b \end{aligned} \tag{42}$$

$$\begin{aligned} M_{sxi} &= -2K_{sy}h_1y_b - 2C_{sy}h_2\dot{y}_b - 2b_1^2K_{pz}\phi_i \\ &\quad - 2b_1^2C_{pz}\dot{\phi}_i \end{aligned} \tag{43}$$

The forces and moments acting on the bogie frame can now be written:

$$\begin{aligned} F_{syb} &= 2K_{py}y_1 + 2C_{py}\dot{y}_1 + 2K_{py}y_2 + 2C_{py}\dot{y}_2 \\ &\quad - (4K_{py} + 2K_{sy})y_b - (4C_{py} + 2C_{sy})\dot{y}_b \end{aligned} \tag{44}$$

$$\begin{aligned} M_{szb} &= 2K_{py}L_1y_1 + 2C_{py}L_2\dot{y}_1 + 2K_{px}b_1^2\psi_1 + 2C_{px}b_1^2\dot{\psi}_1 \\ &\quad - 2K_{py}L_1y_2 - 2C_{py}L_2\dot{y}_2 + 2K_{px}b_1^2\psi_2 + 2C_{px}b_1^2\dot{\psi}_2 \\ &\quad - (4K_{py}L_1^2 + 4K_{px}b_1^2 + 2K_{sx}b_2^2)\psi_b \\ &\quad - (4C_{py}L_2^2 + 4C_{px}b_1^2 + 2C_{sx}b_3^2)\dot{\psi}_b \end{aligned} \tag{45}$$

The wheelset contact flange forces,  $F_{ti}$ , are modelled as a piecewise linear function, being  $\delta$  the existing clearance between the wheel flange and the rail and  $K_r$  is rail stiffness.

$$F_{ti} = \begin{cases} K_r(y_i - \delta), & y_i \geq \delta \\ 0, & -\delta < y_i < \delta \\ K_r(y_i + \delta), & y_i \leq -\delta \end{cases} \tag{46}$$

Finally, by introducing Eqs. (16)–(25) and (37)–(43) into Eqs. (3)–(6) the explicit equations that define the dynamics of the wheelsets are nonlinear and their expressions are as follows:

$$\begin{aligned}
 m_w \ddot{y}_i = & -\frac{2\alpha_{if11}}{V} \dot{y}_i + 2\alpha_{if11} \psi_i - \frac{2\alpha_{if12}}{V} \dot{\psi}_i - W_{pa} \phi_i \\
 & - \frac{2r_0 \alpha_{if11}}{V} \dot{\phi}_i - 2K_{py} y_i - 2C_{py} \dot{y}_i + 2K_{py} y_b \\
 & + 2C_{py} \dot{y}_b - (-1)^i 2K_{py} L_1 \psi_b - (-1)^i 2C_{py} L_2 \dot{\psi}_b - F_{ii}
 \end{aligned} \tag{47}$$

$$\begin{aligned}
 m_w \ddot{z}_i = & -\frac{2\alpha_{if11} \lambda^2}{V} \dot{\phi}_i y_i - \frac{2\alpha_{if11}}{V} \phi_i \dot{y}_i - \frac{2\alpha_{if12}}{V} \phi_i \dot{\psi}_i \\
 & - \frac{2\alpha_{if11} r_0}{V} \phi_i \dot{\phi}_i + \frac{2\alpha_{if12} \lambda^2}{r_0} - 2K_{pz} z_i - 2C_{pz} \dot{z}_i \\
 I_{wz} \ddot{\psi}_i = & \frac{-2e\alpha_{if33} \lambda}{r_0} y_i + \frac{2\alpha_{if12}}{V} \dot{y}_i + (eW_{pa} \lambda - 2\alpha_{if12}) \psi_i \\
 & + \frac{(-2e^2 \alpha_{if33} - 2\alpha_{if22})}{V} \dot{\psi}_i + \left( -\frac{I_{wy} V}{r_0} + \frac{2r_0 \alpha_{if12}}{V} \right) \dot{\phi}_i \\
 & - 2K_{px} b_1^2 \psi_i - 2C_{px} b_1^2 \dot{\psi}_i + 2b_1^2 K_{px} \psi_b + 2C_{px} b_1^2 \dot{\psi}_b
 \end{aligned} \tag{48}$$

$$\begin{aligned}
 = & \frac{2\alpha_{if12} \lambda^4 W_{pa}}{r_0} y_i - \frac{2\alpha_{if11} (r_0 + e\lambda)}{V} \dot{y}_i \\
 & + \left( 2\alpha_{if11} (r_0 + e\lambda) + \frac{2\alpha_{if22} \lambda^2}{r_0} \right) \psi_i \\
 & + \left( \frac{I_{wy} V}{r_0} - \frac{2f_{12} r_0}{V} - \frac{2f_{12a} \lambda}{V} \right) \dot{\psi}_i \\
 & + (2\lambda^2 \alpha_{if12} + e\lambda W_{pa}) \phi_i - \frac{2\alpha_{if11} r_0 (e\lambda + r_0)}{V} \dot{\phi}_i \\
 & - 2K_{sy} h_1 y_b - 2C_{sy} h_2 \dot{y}_b - 2b_1^2 K_{pz} \phi_i - 2b_1^2 C_{pz} \dot{\phi}_i
 \end{aligned} \tag{50}$$

Finally, the equations governing the dynamics of the bogie frame are obtained by substituting Eqs. (44)–(45) into Eqs. (1)–(2):

$$\begin{aligned}
 m_b \ddot{y}_b = & 2K_{py} y_1 + 2C_{py} \dot{y}_1 + 2K_{py} y_2 + 2C_{py} \dot{y}_2 \\
 & + (-4K_{py} - 2K_{py}) y_b + (-4C_{py} - 2C_{py}) \dot{y}_b
 \end{aligned} \tag{51}$$

$$\begin{aligned}
 I_{bz} \ddot{\psi}_b = & 2K_{py} L_1 y_1 + 2C_{py} L_2 \dot{y}_1 + 2K_{px} b_1^2 \psi_1 \\
 & + 2C_{px} b_1^2 \dot{\psi}_1 - 2K_{py} L_1 y_2 - 2C_{py} L_2 \dot{y}_2 + 2K_{px} b_1^2 \psi_2 \\
 & + 2C_{px} b_1^2 \dot{\psi}_2 - (4K_{py} L_1^2 + 4K_{px} b_1^2 + 2K_{sx} b_2^2) \psi_b \\
 & - (4C_{py} L_2^2 + 4C_{px} b_1^2 + 2C_{sx} b_3^2) \dot{\psi}_b.
 \end{aligned} \tag{52}$$

The set of Eqs. (47)–(52) represent the coupled dynamics of the system under study.

### 4 Stability analysis

The EN 14363:2016 + A1:2018 standard [31] sets the acceptable running characteristics and stability standards for railway vehicles. For trains whose maximum running speed is higher than 100 km/h and less or equal to 300 km/h, stability should be kept for all speeds up to at least 10% above the maximum running speed. In the case of trains with a maximum running speed above 300 km/h, stability should be guaranteed (at least) up to speeds 30 km/h above the maximum running speed. In this case, as the maximum speed of this HST is 300 km/h, the train should be stable at least up to  $V = 330$  km/h.

Determining the hunting stability of a railway bogie is key to defining the maximum operating speed of the vehicle. Stability characteristics have a direct impact on ride performance, comfort and, ultimately, safety of these types of vehicles. The hunting speed for the HST is obtained and the stability boundaries are determined by means of time-domain response, eigenvalue analysis and limit cycle characterization.

The ten second-order nonlinear Eqs. (47)–(52) are transformed into a 20th-dimensional system of first-order nonlinear equations of the form:

$$\dot{X} = f(X) = A(X) \tag{53}$$

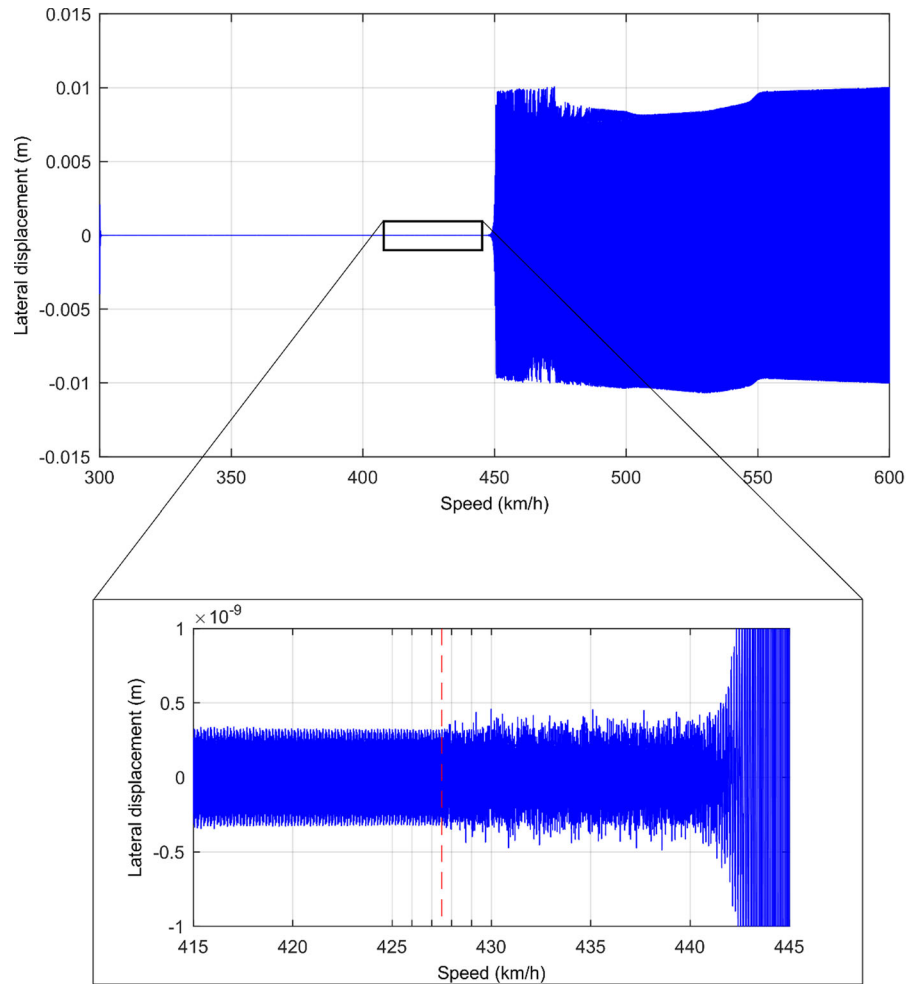
where  $A^{n \times n}$ ,  $n = 20$ , is the system’s matrix containing couplings and nonlinear terms and  $X^{n \times 1}$  is the vector of state’s variables and velocities:

$$\begin{aligned}
 X^T = & \left( y_1, \dot{y}_1, z_1, \dot{z}_1, \psi_1, \dot{\psi}_1, \phi_1, \dot{\phi}_1, y_2, \dot{y}_2, z_2, \dot{z}_2, \right. \\
 & \left. \psi_2, \dot{\psi}_2, \phi_2, \dot{\phi}_2, y_b, \dot{y}_b, \psi_b, \dot{\psi}_b \right)^T
 \end{aligned}$$

Note that expression (53) consists of eight equations corresponding to wheelset 1, eight equations corresponding to wheelset 2 and four equations describing the frame’s dynamics, therefore  $X$  is a vector of ten state variables and ten generalized speeds.

Equations (53) are solved using the Runge–Kutta method implemented in MATLAB® and make use of the HST bogie reference parameters given in Table 1. The function chosen to solve the differential equations is ODE45, it implements the Dormand–Prince method (member of the Runge–Kutta family), and it offers the best relation between accuracy and computation time for this problem.

**Fig. 9** Lateral bogie displacement from initial speed  $v_i = 300$  km/h and zoomed-in details of the unstable region onset



Initial conditions were chosen to represent a bogie travelling at an initial forward speed  $v_i = 300$  km/h slowly increased by a positive acceleration  $a = 0.1$  m/s<sup>2</sup> up to a final speed  $v_f = 600$  km/h. In this way, although the model is nonlinear, at each forward speed the system can be considered as quasi-static and approximated by a matrix  $A$  of constant values. At each time step of the simulation, the system eigenvalues are found, and its complex plane representation is analysed.

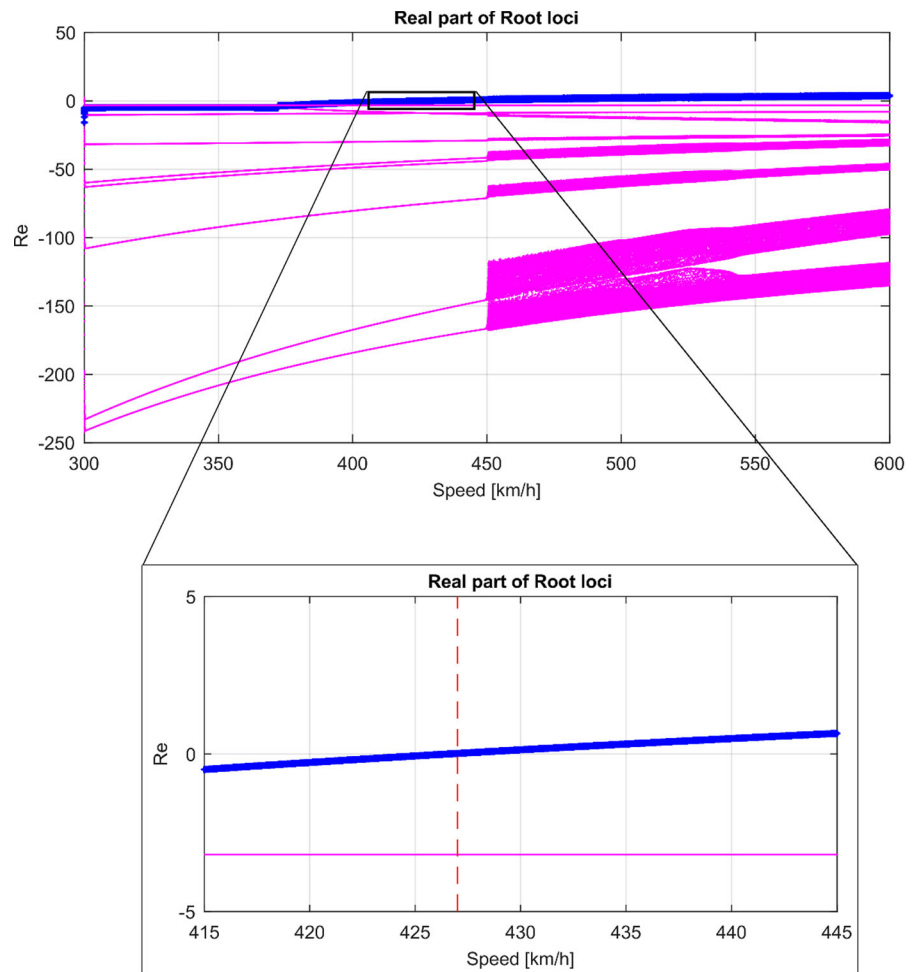
Figure 7 shows the evolution of the system's modes that are near the unstable region when the speed is increased from  $v_i$  up to  $v_f$ . The modes are seen to have different frequencies and all of them are well-damped except for one that crosses the imaginary axis into the unstable region at a speed slightly above 400 km/h, more specifically at 427 km/h. This speed value is the hunting speed (or critical speed  $v_c$ ). When the bogie

forward speed reaches  $v_c$ , this mode becomes undamped and the system is prone to behave in an unstable manner.

Figure 8 shows a closer view of the mode under discussion when it crosses the unstable region. At the lower speed,  $v_i = 300$  m/s (triangle) this mode is on the left-hand side of the complex plane, the system is stable and it becomes less when speed is increased and crosses the imaginary axis at  $v_c = 427$  km/h.

Figure 9 shows the lateral displacement of the bogie when the initial speed is increased. It is clearly seen how the amplitude of this lateral oscillation increases once the critical speed is reached at 427 km/h. Even more, the amplitude shows an increasing tendency which is supported by the mode found to become unstable at that same speed (Fig. 7). The zoomed image between 415 and 445 km/h highlights the instants in which the lateral displacement becomes

**Fig. 10** HST bogie real part of root loci from initial speed  $v_i = 300$  km/h up to  $v_f = 600$  km/h and zoom of the transition to the unstable region



unstable. It is seen how the constant amplitude oscillations start increasing in amplitude until these clearly become unstable.

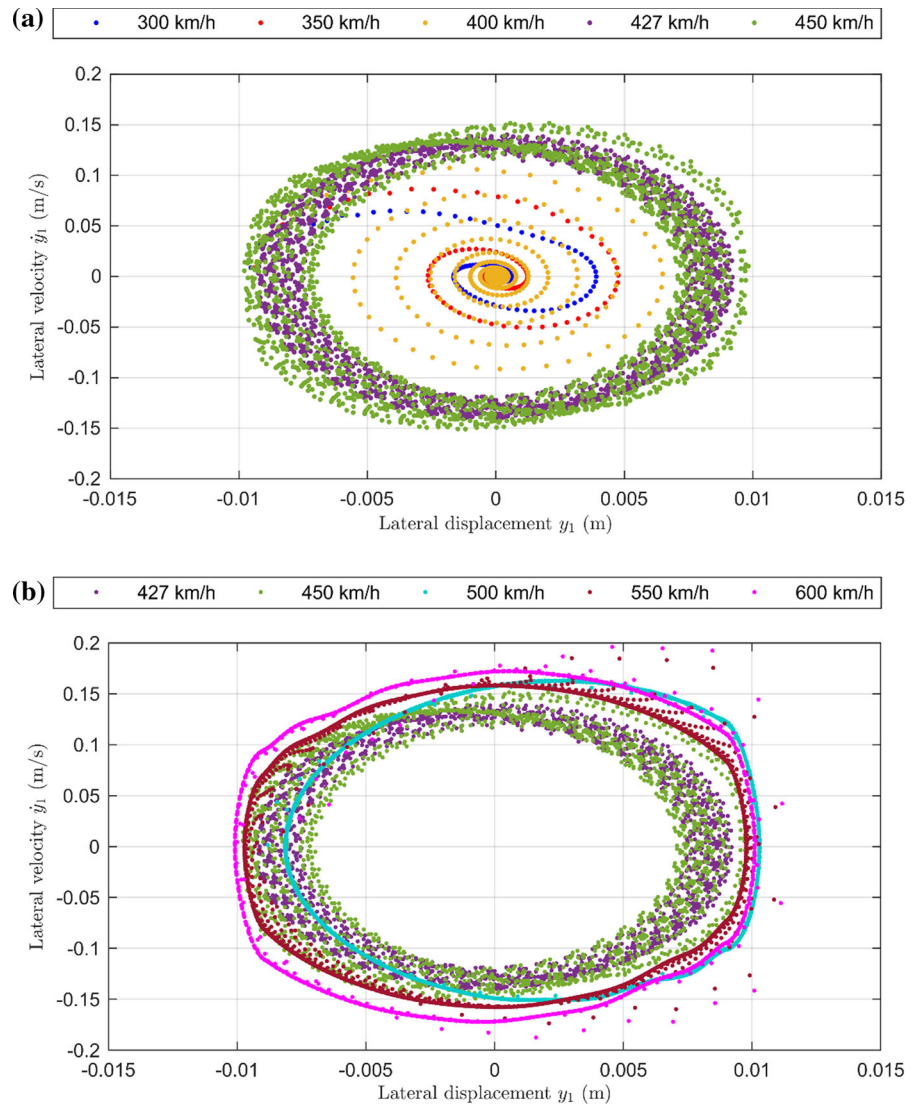
The value of the critical speed  $v_c$  can also be determined by looking at the real part of the root loci modes. There is only one mode whose real part becomes positive (blue trajectory) as can be seen in Fig. 10. The speed at which this mode crosses into the unstable region is 427 km/h. The rest of the modes remain stable (real parts negative) although they show fluctuations in their real part values at speeds just slightly above the hunting speed. This phenomenon is due to the creepage saturation and the reaching of the limit cycle. These fluctuations begin at 450 km/h. At this forward speed, the bogie is experiencing the hunting motion and moving laterally from one rail to the other (see Figs. 9 and 10).

The phase portrait is shown in Fig. 11. It is clearly visible that the system is stable at speeds below the critical speed as the trajectory moves from the initial condition to a stable point located in (0,0). Above the critical speed  $v_c = 427$  km/h, the system describes limit cycles and, therefore, becomes unstable. However, the trajectory of the limit cycles is not well defined until exceeding 450 km/h.

## 5 Sensitivity analysis

This section studies the influence of the axle load and suspension parameters on the critical speed of the bogie. To that end, axle load, primary suspension stiffness (longitudinal, lateral and vertical), primary suspension vertical damping, secondary suspension stiffness (longitudinal and lateral) and secondary

**Fig. 11** HST bogie phase portrait from initial speed  $v_i = 300$  km/h up to  $v_f = 600$  km/h. It is split into two for clarity: from  $v = 300$  to 450 km/h (a) and from 427 to 600 km/h (b)



suspension damping are modified  $\pm 50\%$  from their nominal values.

The critical speed is determined by finding the speed at which the real part of the root locus becomes positive.

Figure 12 shows the evolution of the critical speed as a function of the axle load. It becomes noticeable that the critical speed has a strong dependence on the axle load. The highest critical speed (427 km/h) is reached near the nominal axle load ( $1.5 \cdot 10^5$  -  $N \sim 15$  tons). The lowest critical speed (375 km/h) is obtained when the axle load is low. Increasing the axle load from the nominal value has a similar effect and the critical speed reduces as the axle load

increases. Hence, and according to the results, the bogie is optimized for the nominal axle load.

The influence of the primary suspension parameters is plotted in the graphs in Fig. 13. According to the graphs of the longitudinal and lateral stiffness of the primary suspension, the influence of these parameters on the critical speed value is limited. When varying the longitudinal stiffness (see Fig. 13a), the highest critical speed is obtained for the nominal value. In the lateral stiffness case (see Fig. 13b), the maximal critical speed is achieved for the largest stiffness value.

On the other hand, the vertical stiffness of the primary suspension has a strong influence on the



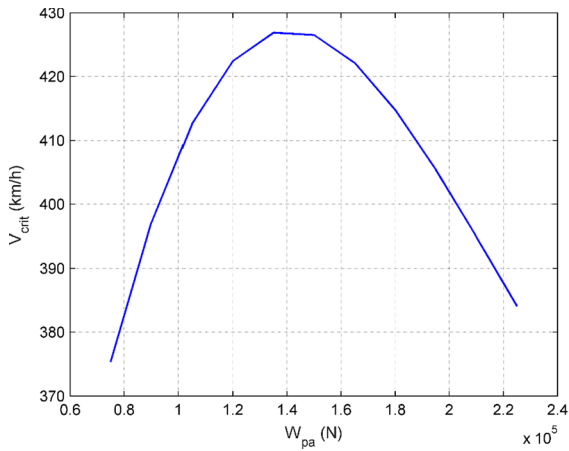
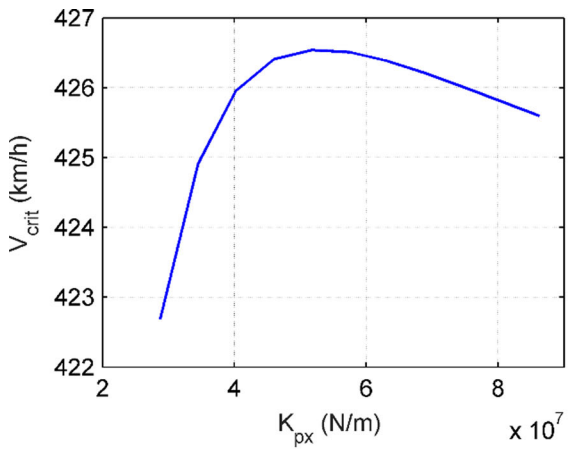


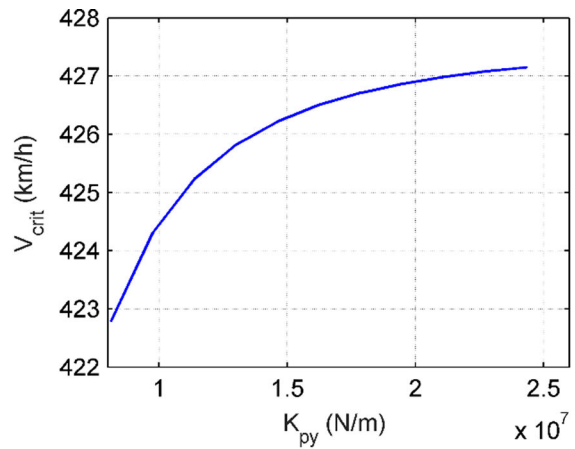
**Fig. 12** Evolution of the critical speed as a function of the axle load

critical speed (see Fig. 13c). Larger stiffness values lead to higher critical speeds (up to 466 km/h). As the trend is to increase the critical speed, exceptionally the sensitivity analysis is enlarged up to 2.5 times the nominal value of the vertical stiffness in order to better analyse the behaviour. Doing this, it is seen that the maximum critical speed (467 km/h) is reached when the stiffness is  $9.1 \times 10^5$  N/m. Then, the critical speed begins to drop.

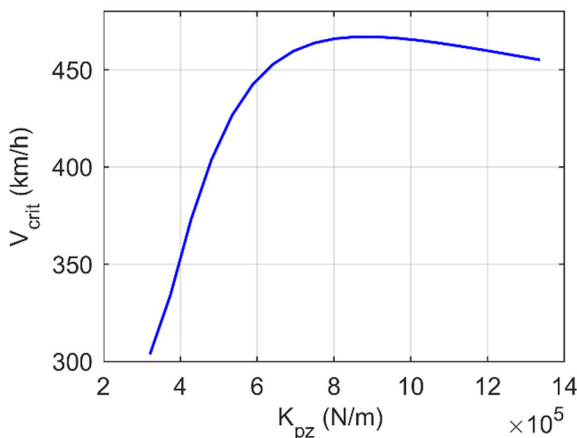
Increasing the vertical damping of the primary suspension (see Fig. 13d) has a negative effect on the bogie’s critical speed: it is lower as the damping becomes larger. However, the speed variation is within 15 km/h, so the influence of the vertical damping is limited.



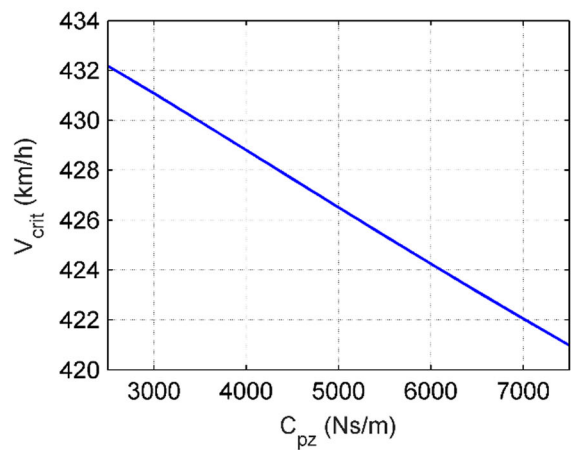
(a)



(b)



(c)



(d)

**Fig. 13** Evolution of the critical speed as a function of primary suspension parameters

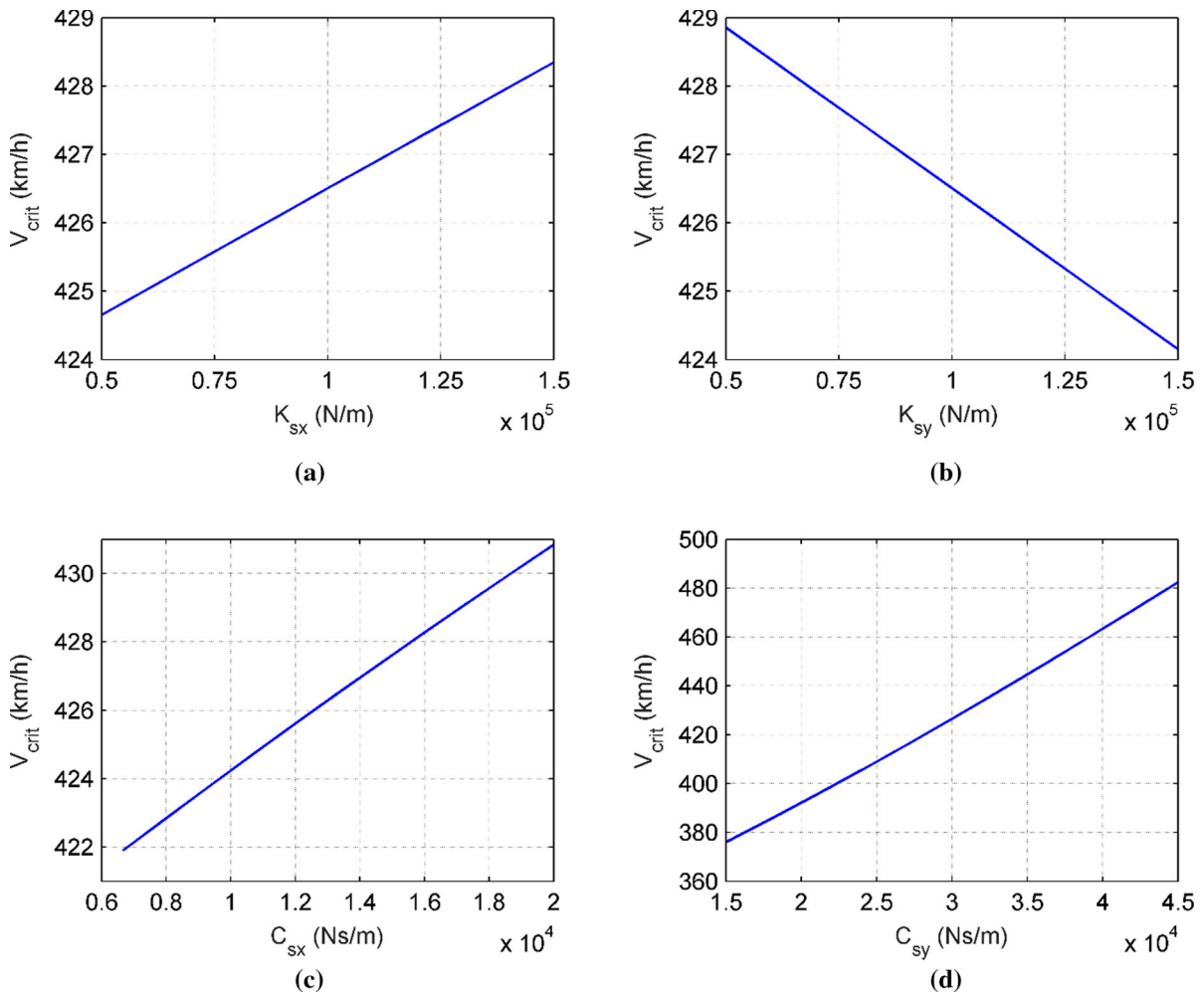


**Fig. 14** Evolution of the critical speed as a function of secondary suspension parameters

The influence of the secondary suspension on the critical speed is plotted in Fig. 14. The longitudinal and lateral stiffnesses, as well as the longitudinal damping, have a small effect on the critical speed (see Fig. 14a–c). Increasing the longitudinal stiffness and damping increases the critical speed while increasing the lateral stiffness decreases the critical speed. However, the maximum critical speed variation observed is about 10 km/h, which is negligible in practice.

On the other hand, modifying the lateral damping of the secondary suspension changes significantly the critical speed (see Fig. 14d). This is reduced to only 376 km/h for the lowest damping and increased up to 482.5 km/h for the largest damping. Therefore, and according to these results, the largest available lateral

damping should be set when designing a high-speed train.

The nine parameters mentioned at the beginning of this section are also analysed in pairs, which lead to 36 possible parameter combinations. For readability reasons, they will be only discussed the results of crossing the axle load with the primary suspension parameters, the stiffness and damping coefficients when available and the primary suspension vertical stiffness with the secondary suspension lateral damping, as these parameters have the strongest influence on the critical speed.

Figure 15 shows the performance of the critical speed when the axle load and the parameters of the primary suspension are changed at the same time.

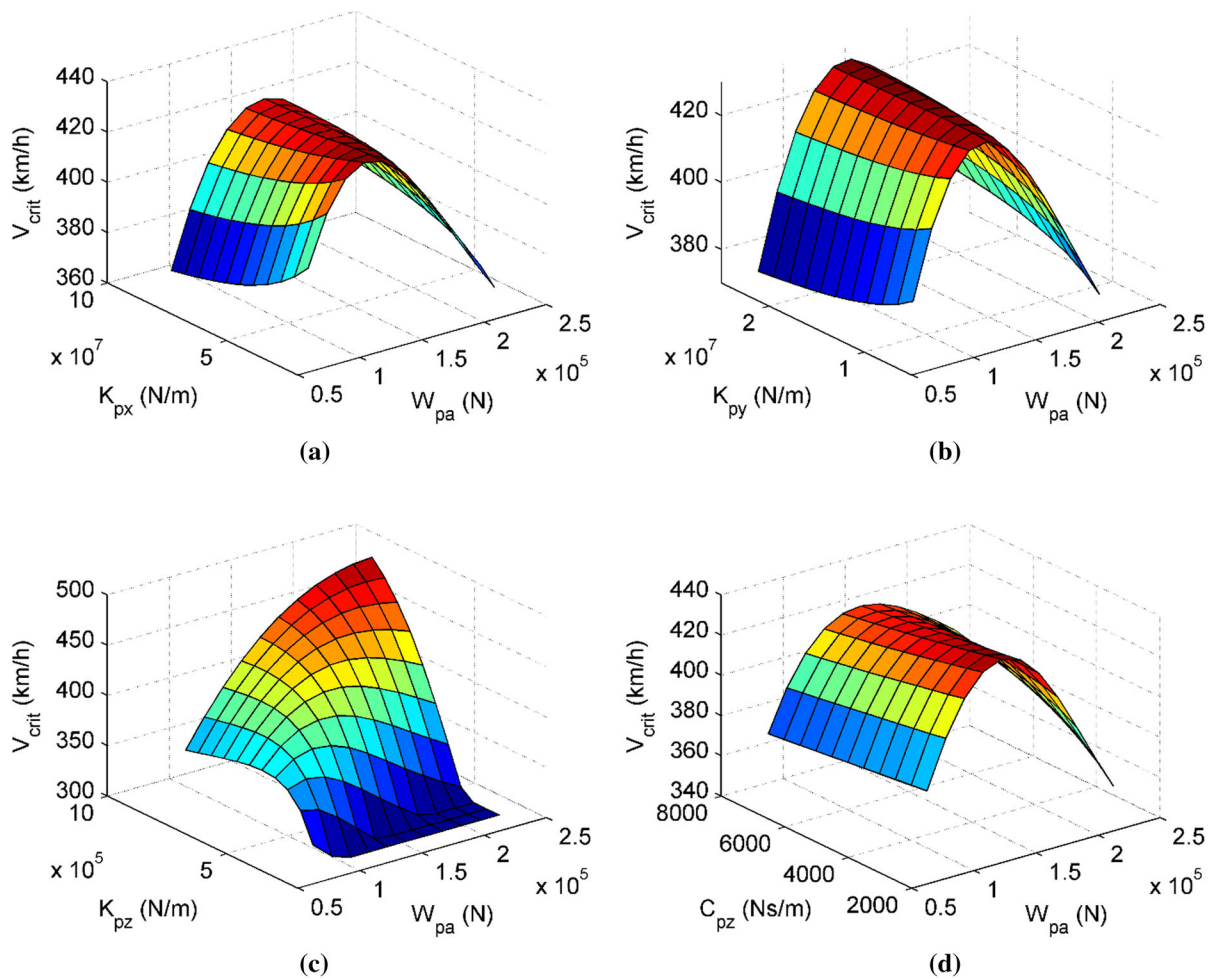


**Fig. 15** Evolution of the critical speed as a function of axle load and primary suspension parameters

As was mentioned above when examining the parameters individually, the longitudinal and lateral stiffness and the vertical damping of the primary suspension have a small effect on the critical speed. Therefore, the shape of the resulting surface is driven basically by the axle load. The highest critical speeds are obtained for medium values of the axle load and the largest longitudinal stiffness in one case (see Fig. 15a), and the lowest lateral stiffness (Fig. 15b) and vertical damping (Fig. 15d), in the other two.

On the other hand, the result of changing simultaneously the axle load and the vertical stiffness leads to a great increase in the critical speed as both parameters become larger (see Fig. 15c). Consequently, and according to the results, the best strategy to increase the critical speed of the bogie will be to raise the axle

load and stiff the vertical springs of the primary suspension as much as possible.

Figure 16 displays the results of changing at the same time the stiffnesses and dampings of the suspension.

The simultaneous variation of the longitudinal parameters (see Fig. 16a) of the secondary suspension results in a maximum critical speed of 432.7 km/h when the larger stiffness and damping are used, which is near the nominal critical speed and, therefore, there is no strong effect on the critical speed.

However, varying the vertical primary suspension and the lateral secondary suspension alters significantly the value of the critical speed. Regarding the lateral secondary suspension, it is observed a constant increment of the critical speed as the damping

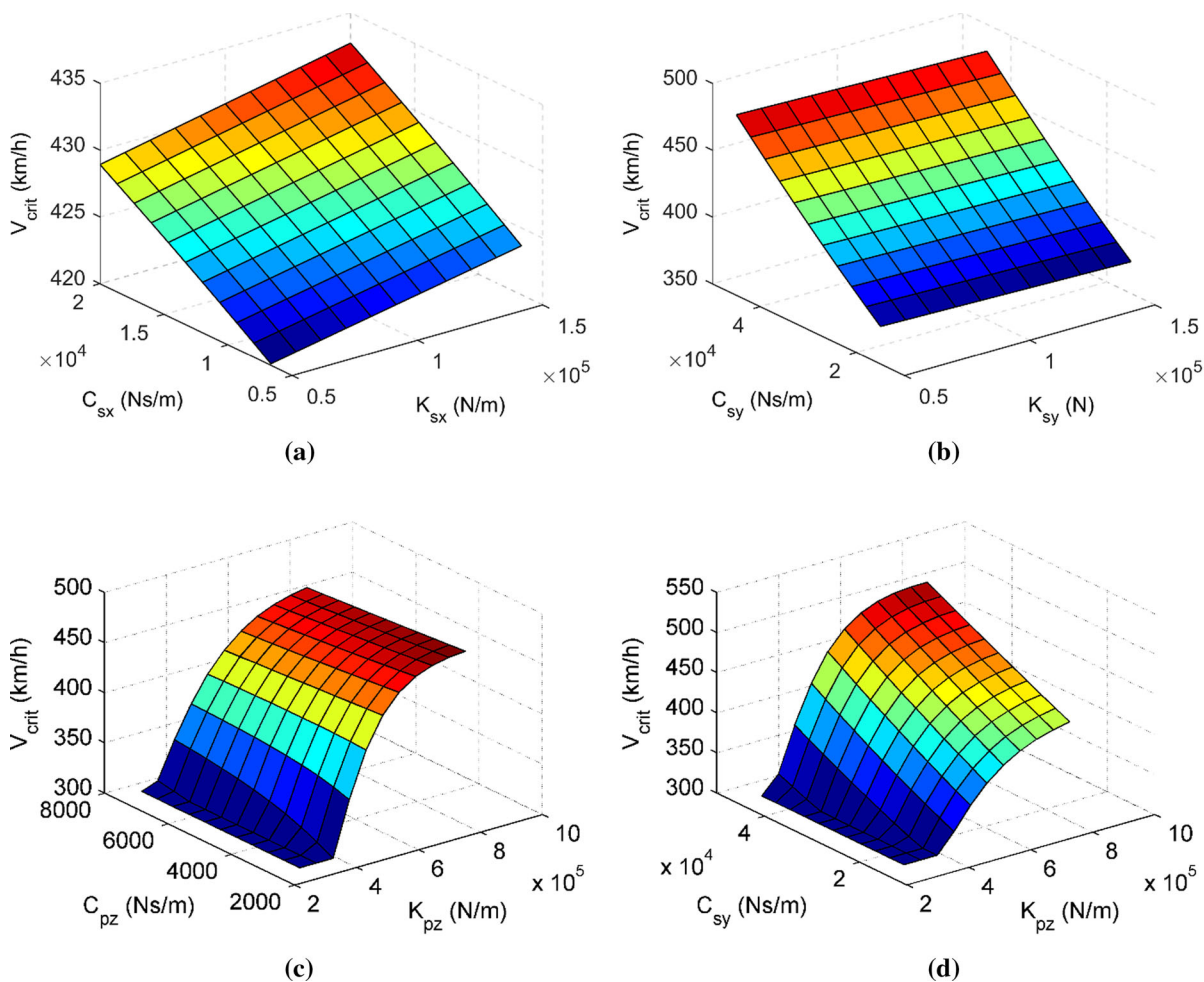


**Fig. 16** Evolution of the critical speed as a function of suspension parameters

becomes greater. Indeed, the highest critical speed is achieved for the largest damping and the lowest stiffness (Fig. 16b). What concerns the vertical primary suspension, the main contribution to increasing the critical speed is due to the stiffness. The maximum critical speed is achieved for the biggest stiffness and the lowest damping (Fig. 16c).

The combination of the vertical stiffness of the primary suspension and the lateral damping of the secondary suspension (Fig. 16d) allows achieving the highest critical speed of all possible combinations. This is reached when the biggest value of both the vertical stiffness and lateral damping is selected. Hence, the best way to obtain a higher critical speed for a given axle load would be to increase the stiffness of the vertical springs in the primary suspension and

the damping of the secondary suspension lateral dampers as much as possible.

The specific values at which the highest or maximum critical speed is achieved are summarized in Table 2.

## 6 Conclusions

The paper presents a nonlinear model of a high-speed bogie with 10 degrees of freedom. The model will be the first step in the development of a Digital Twin of the high-speed train for maintenance purposes. Simulations are performed at travelling speeds from 300 up to 600 km/h. The stability of the system is studied using the root loci criterion and verified through the lateral displacement of the wheelset and the phase

**Table 2** Maximum critical speed for different parameter combinations

Parameter 1		Parameter 2		Max critical speed (km/h)
Name	Value	Name	Value	
$W_{pa}$	$1.2 \times 10^5$ N	$K_{px}$	$2.875 \times 10^7$ N/m	430.7
$W_{pa}$	$1.5 \times 10^5$ N	$K_{py}$	$2.438 \times 10^7$ N/m	427.2
$W_{pa}$	$2.25 \times 10^5$ N	$K_{pz}$	$8.021 \times 10^5$ N/m	498.9
$W_{pa}$	$1.35 \times 10^5$ N	$C_{pz}$	$2.5 \times 10^3$ Ns/m	435.2
$K_{sx}$	$1.5 \times 10^5$ N/m	$C_{sx}$	$2 \times 10^4$ Ns/m	432.7
$K_{sy}$	$5 \times 10^4$ N/m	$C_{sy}$	$4.5 \times 10^4$ Ns/m	485.1
$K_{pz}$	$8.021 \times 10^5$ N/m	$C_{pz}$	$2.5 \times 10^3$ Ns/m	472.6
$K_{pz}$	$8.021 \times 10^5$ N/m	$C_{sy}$	$4.5 \times 10^4$ Ns/m	511.3

portrait. The critical speed is established by identifying the travelling speed at which one of the modes of the root loci crosses into the unstable region.

For nominal conditions, the behaviour of the system is as follows:

- The system is stable below the critical speed
- The system becomes unstable after exceeding the critical speed, but the lateral displacements of the bogie are small between the critical speed (427 km/h) and 447 km/h.
- Above 450 km/h, the lateral displacements become larger in amplitude and the bogie experiences hunting motion.

In addition to the above, a sensitivity study is also carried out in order to determine which suspension components have the greatest effect on the bogie's stability and, hence, on safety. The results of this study show that the axle load, the primary suspension vertical stiffness and the secondary suspension lateral damping have a significant influence on the critical speed: the variation exceeds 100 km/h in some cases. Clearly, these parameters should be constantly monitored to ensure that potential degradation of primary vertical springs and secondary lateral dampers do not yield a considerable low critical speed that could compromise the safety of the high-speed train. The remainder of the parameters studied in this work has been found to barely influence the critical speed (variations of less than 15 km/h).

The influence of the axle load on the critical speed has a great interest too. The suspension parameters are parameters that in the case of suffering any variation, it happens slowly. On the other hand, the axle load is a variable parameter that is highly dependent on the passengers and luggage carried. Under extreme

conditions, a stable railway vehicle could become unstable if there were too many or too few passengers inside the vehicle.

Simulation results obtained are consistent with the performance of the high-speed train, as the achieved critical speed (427 km/h for nominal parameters) is beyond the speed at which the train was homologated (300 km/h) and the maximum speed it reached during tests (356 km/h). Roller rig test bench experiments will be carried out in the future to validate the current model.

**Acknowledgements** The research work described in this paper is part of the R&D and Innovation projects MC4.0 PID2020-116984RB-C21 and MC4.0 PID2020-116984RB-C22 supported by the MCIN/AEI/10.13039/501100011033 and by the Universidad Carlos III de Madrid through the "Ayudas para la movilidad de investigadores de la UC3M en centros de investigación nacionales y extranjeros en sus dos modalidades 2019" project.

**Funding** Open Access funding provided thanks to the CRUE-CSIC agreement with Springer Nature.

#### Declarations

**Conflict of interest** The authors declare no conflict of interest.

**Data availability** All data generated or analysed during this study are included in this published article [and its supplementary information files].

**Open Access** This article is licensed under a Creative Commons Attribution 4.0 International License, which permits use, sharing, adaptation, distribution and reproduction in any medium or format, as long as you give appropriate credit to the original author(s) and the source, provide a link to the Creative Commons licence, and indicate if changes were made. The images or other third party material in this article are included in the article's Creative Commons licence, unless indicated otherwise in a credit line to the material. If material is not



included in the article's Creative Commons licence and your intended use is not permitted by statutory regulation or exceeds the permitted use, you will need to obtain permission directly from the copyright holder. To view a copy of this licence, visit <http://creativecommons.org/licenses/by/4.0/>.

## References

- Directorate-General for Mobility and Transport (European Commission): EU transport in figures: statistical pocket-book 2020. Publications Office of the European Union, LU (2020)
- Sun, X., Zhang, Y., Wandelt, S.: Air transport versus high-speed rail: an overview and research agenda. *J. Adv. Transp.* **2017**, 1–18 (2017). <https://doi.org/10.1155/2017/8426926>
- Prussi, M., Lonza, L.: Passenger aviation and high speed rail: a comparison of emissions profiles on selected European routes. *J. Adv. Transp.* **2018**, 1–10 (2018). <https://doi.org/10.1155/2018/6205714>
- Wickens, A.H.: *Fundamentals of Rail Vehicle Dynamics*. Swets & Zeitlinger B.V., Lisse (2003)
- Polach, O.: On non-linear methods of bogie stability assessment using computer simulations. *Proc. Inst. Mech Eng. Part F J. Rail Rapid Transit.* **220**, 13–27 (2006). <https://doi.org/10.1243/095440905X33251>
- Schupp, G.: Bifurcation analysis of railway vehicles. *Multibody Syst. Dyn.* **15**, 25–50 (2006). <https://doi.org/10.1007/s11044-006-2360-6>
- Zboinski, K., Dusza, M.: Bifurcation analysis of 4-axle rail vehicle models in a curved track. *Nonlinear Dyn.* **89**, 863–885 (2017). <https://doi.org/10.1007/s11071-017-3489-y>
- Rezvani, M.A., Mazraeh, A.: Dynamics and stability analysis of a freight wagon subjective to the railway track and wheelset operational conditions. *Eur. J. Mech. A Solids* **61**, 22–34 (2017). <https://doi.org/10.1016/j.euromechsol.2016.08.011>
- Wickens, A.H.: The dynamic stability of railway vehicle wheelsets and bogies having profiled wheels. *Int. J. Solids Struct.* **1**, 319–341 (1965). [https://doi.org/10.1016/0020-7683\(65\)90037-5](https://doi.org/10.1016/0020-7683(65)90037-5)
- Ahmadian, M., Yang, S.: Effect of system nonlinearities on locomotive bogie hunting stability. *Veh. Syst. Dyn.* **29**, 365–384 (1998). <https://doi.org/10.1080/00423119808969380>
- Choi, Y.-S., Shin, B.-S.: Critical speed of high-speed trains considering wheel-rail contact. *J. Mech. Sci. Technol.* **29**, 4593–4600 (2015). <https://doi.org/10.1007/s12206-015-1004-2>
- Yan, Y., Zeng, J.: Hopf bifurcation analysis of railway bogie. *Nonlinear Dyn.* **92**, 107–117 (2018). <https://doi.org/10.1007/s11071-017-3634-7>
- Horak, D., Wormley, D.N.: Nonlinear stability and tracking of rail passenger trucks. *J. Dyn. Syst. Meas. Control.* **104**, 256 (1982). <https://doi.org/10.1115/1.3139705>
- Hirotsu, T., Terada, K., Hiraishi, M., Yui, S.: Simulation of Hunting of rail vehicles. The case using a compound circular wheel profile. *JSME Int. J. Ser. 3 Vib. Control Eng. Eng. Ind.* **34**, 396–403 (1991). <https://doi.org/10.1299/jsmec1988.34.396>
- Lee, S.-Y., Cheng, Y.-C.: Hunting stability analysis of high-speed railway vehicle trucks on tangent tracks. *J. Sound Vib.* **282**, 881–898 (2005). <https://doi.org/10.1016/j.jsv.2004.03.050>
- Cheng, Y.-C., Lee, S.-Y., Chen, H.-H.: Modeling and non-linear hunting stability analysis of high-speed railway vehicle moving on curved tracks. *J. Sound Vib.* **324**, 139–160 (2009). <https://doi.org/10.1016/j.jsv.2009.01.053>
- Yao, Y., Li, G., Sardahi, Y., Sun, J.-Q.: Stability enhancement of a high-speed train bogie using active mass inertial actuators. *Veh. Syst. Dyn.* **57**, 389–407 (2019). <https://doi.org/10.1080/00423114.2018.1469776>
- Sun, J., Chi, M., Cai, W., Jin, X.: Numerical investigation into the critical speed and frequency of the hunting motion in railway vehicle system. *Math. Probl. Eng.* **2019**, 1–15 (2019). <https://doi.org/10.1155/2019/7163732>
- Zhang, T., Dai, H.: On the nonlinear dynamics of a high-speed railway vehicle with nonsmooth elements. *Appl. Math. Model.* **76**, 526–544 (2019). <https://doi.org/10.1016/j.apm.2019.06.027>
- Guo, J., Shi, H., Luo, R., Zeng, J.: Bifurcation analysis of a railway wheelset with nonlinear wheel-rail contact. *Nonlinear Dyn.* **104**, 989–1005 (2021). <https://doi.org/10.1007/s11071-021-06373-8>
- Bosso, N., Gugliotta, A., Soma, A.: Multibody simulation of a freight bogie with friction dampers. In: *ASME/IEEE Joint Railroad Conference*, pp. 47–56. ASME, Washington, DC (2002)
- Molatefi, H., Hecht, M., Kadivar, M.H.: Critical speed and limit cycles in the empty Y25-freight wagon. *Proc. Inst. Mech. Eng. Part F J. Rail Rapid Transit.* **220**, 347–359 (2006). <https://doi.org/10.1243/09544097JRR67>
- Knothe, K., Böhm, F.: History of stability of railway and road vehicles. *Veh. Syst. Dyn.* **31**, 283–323 (1999). <https://doi.org/10.1076/vesd.31.5.283.8362>
- True, H.: Railway vehicle chaos and asymmetric hunting. *Veh. Syst. Dyn.* **20**, 625–637 (1992). <https://doi.org/10.1080/00423119208969427>
- Ceruti, A., Marzocca, P., Liverani, A., Bil, C.: Maintenance in Aeronautics in an Industry 4.0 Context: the role of AR and AM. In: *Transdisciplinary Engineering Methods for Social Innovation of Industry 4.0*, p. 10. IOS Press (2018)
- Garg, V.K., Dukkipati, R.V.: *Dynamics of Railway Vehicle Systems*. Academic Press, New York (1984)
- Hertz, H.R.: Über die Berührung fester elastischer Körper. *J. Für Reine Angew. Math.* **92**, 156–171 (1882)
- Shabana, A.A., Zaazaa, K.E., Sugiyama, H.: *Railroad Vehicle Dynamics: A Computational Approach*. CRC Press, Boca Raton (2008)
- Meymand, S.Z., Keylin, A., Ahmadian, M.: A survey of wheel-rail contact models for rail vehicles. *Veh. Syst. Dyn.* **54**, 386–428 (2016). <https://doi.org/10.1080/00423114.2015.1137956>
- Shen, Z.Y., Hedrick, J.K., Elkins, J.A.: A comparison of alternative creep force models for rail vehicle dynamic analysis. *Veh. Syst. Dyn.* **12**, 79–83 (1983). <https://doi.org/10.1080/00423118308968725>
- EN 14363:2016+A1:2018 Railway applications—Testing and Simulation for the acceptance of running characteristics

of railway vehicles-Running Behaviour and stationary tests  
(2016)

**Publisher's Note** Springer Nature remains neutral with regard to jurisdictional claims in published maps and institutional affiliations.

Springer Nature or its licensor holds exclusive rights to this article under a publishing agreement with the author(s) or other rightsholder(s); author self-archiving of the accepted manuscript version of this article is solely governed by the terms of such publishing agreement and applicable law.